ARTICLE

Check for updates

Many-body quantum muon effects and quadrupolar coupling in solids

Matjaž Gomilšek [1,2,3✉], Francis L. Pratt [4], Stephen P. Cottrell [4], Stewart J. Clark [3] & Tom Lancaster [3]

Strong quantum zero-point motion (ZPM) of light nuclei and other particles is a crucial aspect of many state-of-the-art quantum materials. However, it has only recently begun to be explored from an ab initio perspective, through several competing approximations. Here we develop a unified description of muon and light nucleus ZPM and establish the regimes of anharmonicity and positional quantum entanglement where different approximation schemes apply. Via density functional theory and path-integral molecular dynamics simulations we demonstrate that in solid nitrogen, α-N$_2$, muon ZPM is both strongly anharmonic and many-body in character, with the muon forming an extended electric-dipole polaron around a central, quantum-entangled [N$_2$-μ-N$_2$]$^+$ complex. By combining this quantitative description of quantum muon ZPM with precision muon quadrupolar level-crossing resonance experiments, we independently determine the static ^{14}N nuclear quadrupolar coupling constant of pristine α-N$_2$ to be –5.36(2) MHz, a significant improvement in accuracy over the previously-accepted value of –5.39(5) MHz, and a validation of our unified description of light-particle ZPM.

[1] Jožef Stefan Institute, Jamova c. 39, SI-1000 Ljubljana, Slovenia. [2] Faculty of Mathematics and Physics, University of Ljubljana, Jadranska u. 19, SI-1000 Ljubljana, Slovenia. [3] Department of Physics, Durham University, South Road, Durham DH1 3LE, UK. [4] ISIS Muon Group, Science and Technology Facilities Council (STFC), Didcot OX11 0QX, UK. ✉email: matjaz.gomilsek@ijs.si

Quantum zero-point motion (ZPM) of nuclei plays a pivotal role in the structure and dynamics of many important classes of materials, especially those containing light atoms such as hydrogen or lithium[1–3]. Prominent examples of this include recent record high-T_c hydride superconductors[4–10], record-density hydrogen storage materials[11], metallic and solvated Li and F[12,13], as well as many hydrogen-bonded materials[2], e.g., water ice. Outside nuclear quantum effects, ZPM should be even more pronounced for implanted muons μ^+, which act as sensitive probes in muon spin relaxation (μSR) experiments[14–16], since a muon has just 1/9 of the proton mass. We expect a large muon zero-point energy ZPE $\propto m_\mu^{-1/2} \sim 0.7$ eV[15,17–22], corresponding ZPM delocalization $\Delta x \propto m_\mu^{-1/4} \sim 0.2$ Å around isolated muon stopping sites, the merging of candidate muon sites separated by low energy barriers, quantum tunneling, diffusion, and even muon Bloch waves[23,24]. Beyond these, many-body quantum effects like positional entanglement between muons and nuclei are also expected. Muon ZPM challenges the approach of predicting muon stopping sites and the lattice distortions around them using ab initio methods, often based on density functional theory (DFT)[17–19,25], that treats the muon and nuclei as classical particles. Several schemes for approximating muon ZPM have been developed[18,19], mainly divisible into: (i) adiabatic methods, based on a single-particle description[22,26–29], and (ii) harmonic approximations[20,30,31]. Studies of quantum muons using computationally more demanding, but numerically-exact, path-integral molecular dynamics (PIMD) have remained rather sparse[1,24,32], despite its popularity in describing light-nuclei systems[1–3].

Here we develop a unified description of muon and light nuclei ZPM and the regimes in which particular approximations apply, via a DFT+PIMD study of muon ZPM in solid nitrogen, α–N_2 (Fig. 1a and Supplementary Fig. 1a). We characterize the regimes by the degree of (i) anharmonicity and (ii) muon–nuclear positional entanglement, the latter quantified with easy-to-calculate entanglement witnesses[33–35]. We find that in α–N_2 anharmonic many-body quantum effects dominate, as anticipated from previous experimental[23] and theoretical work[36], and discover that an extended electric-dipole polaron of polarized N_2 molecules forms around a central $[N_2$–μ–$N_2]^+$ complex (Fig. 1b). By applying these insights to our precision muon quadrupolar level-crossing resonance (QLCR)[37–39] experiments, we derive an independent estimate of the static nuclear quadrupolar coupling constant (NQCC) of ^{14}N with significantly improved accuracy compared to the literature value[40].

Results

Classical muon. Within the classical, point-particle description of muons and nuclei using DFT, we find a single stable muon site at almost exactly the (0, 1/4, 1/4) position (Fig. 1b and Supplementary Fig. 1b), which lies between two molecules of pristine α–N_2 but is not symmetric under its $Pa\bar{3}$ space group[41,42]. In line with ab initio simulations of muons[36] and protons[43–47] in N_2 clusters, we find that in crystalline α–N_2 a muon forms an almost-linear, almost-centrosymmetric $[N_2$–μ–$N_2]^+$ complex oriented along the [0, 1, 1] direction. Within this complex the muon's bare positive charge $+e_0$ is screened to just $+0.46e_0$ by electrons covalently shared with the two nearest N_2 molecules, leaving them with an electron density deficit and thus a net positive charge of $+0.27e_0$ each ($+0.04e_0$ on the two nearest N atoms and $+0.23e_0$ on the two further-away ones; Fig. 1b and Supplementary Fig. 2). Moreover, we find that an unusual, extended electric-dipole polaron forms around this complex, where its positive charge further induces electric dipole moments (Fig. 1c)

on other, net neutral nearby N_2 molecules (Supplementary Fig. 2) and causes them to reorient to point towards the complex. Up to ~4 Å from the muon, dipolar electrostatic interactions of polarized N_2 molecules with the $[N_2$–μ–$N_2]^+$ complex thus overwhelm the weak electric quadrupole and van der Waals (VdW) N_2–N_2 interactions of pristine α–N_2[40,48].

Single-particle quantum approximations. To incorporate quantum effects we first employ single-particle, adiabatic approximations of muon–nuclear ZPM. Though elaborate schemes have been proposed[22,29], the simplest are weakly- and strongly-bound muon approximations[26–28], corresponding to zero or maximal muon–nuclear entanglement, respectively. In both schemes, an effective single-particle muon potential $V_{eff}(\delta x)$ is constructed from total DFT energy under muon displacements δx from its classical site, while: (i) keeping the nuclei fixed at the positions corresponding to the unperturbed muon site (weakly-bound case), or (ii) letting them relax by $\delta\tilde{r}_N(\delta x)$ to new lowest-energy positions for each δx (strongly-bound case) while keeping the center of mass fixed. Respectively, this corresponds to: (i) assuming independent muon and nuclear ZPM [i.e., a separable muon–nuclear wave-function, $\psi(\delta x, \delta r_N) = \psi_\mu(\delta x)\psi_N(\delta r_N)$] in the weakly-bound case, or (ii) ZPM where a quantum measurement of the muon displacement δx would simultaneously also determine all nuclear displacements δr_N [i.e., a maximally-entangled muon–nuclear wavefunction, $\psi(\delta x, \delta r_N) \propto \psi_\mu(\delta x)\delta(\delta r_N - \delta\tilde{r}_N(\delta x))$, where δ is the Dirac delta function] in the strongly-bound case. Although, by the variational principle, the strongly-bound potential is shallower than the weakly-bound potential (which would tend to increase muon delocalization), the effective mass m_{eff} in the strongly-bound case increases above the free-muon mass m_μ due to additional movement of nuclei with the muon (which would tend to decrease muon delocalization), meaning that muon ZPM delocalization can either increase or decrease in the strongly-bound case. Explicitly, assuming a linear dependence of the displacement of the ith nucleus of mass m_i on the muon displacement, i.e., $\delta\tilde{r}_{Ni}(\delta x) = A_i\delta x$ where A_i is a tensor, the effective mass tensor in the strongly-bound case is given by $m_{eff} = m_\mu \text{id} + \sum_i m_i A_i^T A_i$ where id is the identity tensor. In the weakly-bound case, $m_{eff} = m_\mu$. Once $V_{eff}(\delta x)$ and m_{eff} are known, a single-particle Schrödinger equation for the muon wavefunction $\psi_\mu(\delta x)$, $[-\hbar^2/(2m_{eff})]\nabla^2\psi_\mu + V_{eff}\psi_\mu = (\text{ZPE})\psi_\mu$, can be numerically solved to obtain the muon–nuclear ZPM, encoded in $\psi_\mu(\delta x)$, and the corresponding ZPE. This inherently single-particle approximation with 3 degrees of freedom in δx (due to the assumed zero or maximal muon–nuclear entanglement) cannot describe many-body ZPM involving more than 3 degrees of freedom (i.e., cases with partial muon–nuclear entanglement).

Figures 2a, b show the calculated weakly- and strongly-bound adiabatic effective potentials. Separable potentials are assumed with one eigenaxis, L ∥ [0, 1, 1], along the $[N_2$–μ–$N_2]^+$ complex and two, T_1 ∥ [0, 1, $\bar{1}$] and T_2 ∥ [0, 0, 1], transverse to it, coinciding with muon Γ-point normal mode directions from DFT (Fig. 2c). Table 1 lists the total muon ZPE $= \sum_j$ZPE$_j$ with directional contribution ZPE$_j$ and muon wavefunction widths $\Delta x_j = \langle \delta x_j^2 \rangle^{1/2}$ along the $j =$ L, T_1, and T_2 directions under both approximations. In the weakly-bound case, we find muon ZPM delocalization of 0.16–0.20 Å, which is significant compared to the 1.29(1) Å distance between the classical muon site and the nearest nitrogen. However, in the strongly-bound case we also find large directional effective muon mass renormalization $m_{eff,j}/m_\mu$ due to strong electrostatic interactions within the $[N_2$–μ–$N_2]^+$ complex and with the surrounding polaron, which leads to a large number of nitrogen nuclei following the displaced muon (up to $494m_\mu$ in the complex and a further $494m_\mu$ just in first shell of the polaron). This
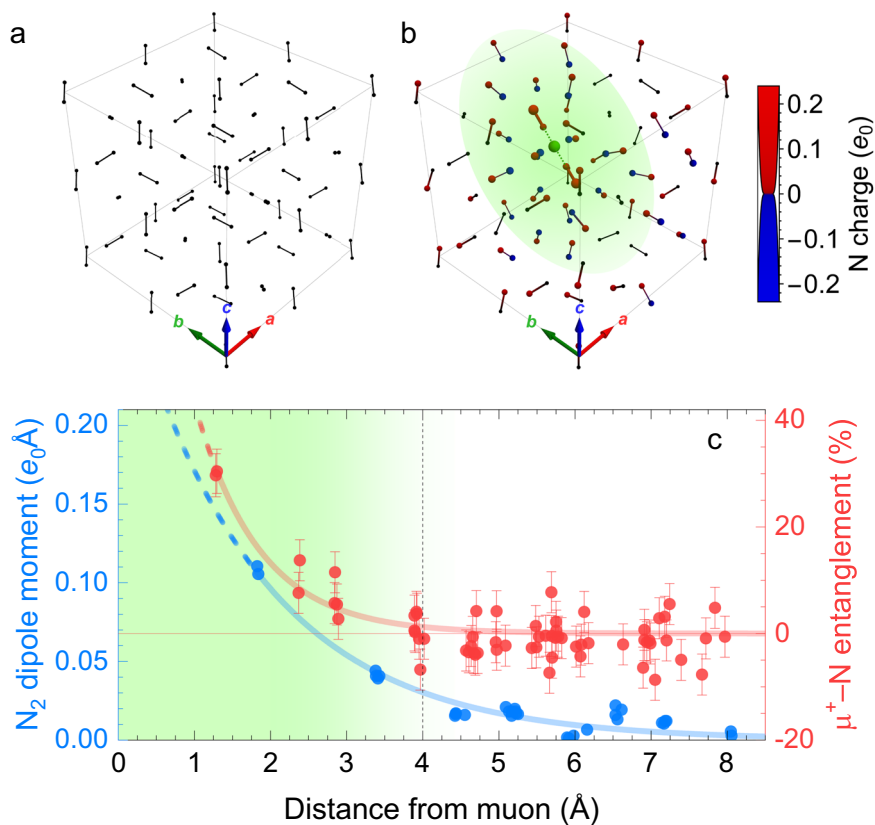
Fig. 1 Muon site and muon–nuclear entanglement. a Pristine α–N_2 crystal structure in a $2 \times 2 \times 2$ supercell. See also Supplementary Movie 1. **b** Classical muon μ^+ (green) in α–N_2 induces an electric-dipole polaron (shading) around a linear $[N_2$–μ–$N_2]^+$ complex. Sphere size/color gives the induced Mulliken charge of nitrogen ions. See also Supplementary Movie 2. **c** Induced N_2 Mulliken electric dipole moments (blue) and degree of muon-nuclear positional entanglement c [Eq. (1)] from path-integral molecular dynamics (PIMD; red). Solid lines are exponential fits, dashed line/shading indicates the polaron size. c error bars represent a systematic uncertainty of one standard deviation (see Methods).

leads to a significantly reduced ZPE and delocalization (Table 1) under the strongly-bound approximation, despite a shallower effective potential (Fig. 2a, b) compared to the weakly-bound case.

Toy model. Given the discrepancy between the two adiabatic approximations, the question of their applicability arises In other words, whether muon–nuclear ZPM is minimally (weakly-bound limit), maximally (strongly-bound limit), or partially entangled. We address this using a toy model with the muon bound to $N = 2$ nearby effective nuclei with force constants k_μ, which are further bound to a static lattice with force constants k_n. If $k_\mu \ll k_n$ muon displacements barely perturb the nuclei (weakly-bound limit), while if $k_\mu \gg k_n$ muon displacements strongly displace nearby nuclei (strongly-bound limit). We estimate the ratio k_μ/k_n in α–N_2 from the ratio of adiabatic potentials as $k_{\mu,j}/k_{n,j} = V_{\text{eff}}^{\text{weak}}/V_{\text{eff}}^{\text{strong}} - 1 \approx 7, 12$, and 9 along the $j = L, T_1$, and T_2 directions, respectively (Fig. 2a, b). This excludes the weakly- but not the strongly-bound adiabatic approximation. However, the relatively large ratio k_μ/k_n still competes with the tendency of light particles to partially positionally decouple from heavier particles[23], which could lead to an intermediate, partially-entangled regime where single-particle (adiabatic) approximations fail. This is tendency is expected to be further reinforced by the enhanced mass $m_{n,j}$ of effective nearest nuclei in the toy model needed to obtain the same calculated effective muon mass $m_{\text{eff},j}$ under the strongly-bound adiabatic approximation both from DFT (Table 1) and from the toy model. Namely, in the toy model we need $m_{n,j} = (1 + k_{n,j}/k_{\mu,j})^2(m_{\text{eff},j} - m_\mu)/N = 4.2(9)m_N, 1.7(2)m_N$, and $2.6(4)m_N$ along the $j = L, T_1$, and T_2 directions, respectively, where m_N is the mass of a nitrogen nucleus.

Harmonic quantum approximations. An alternative class of approximations are harmonic methods[20,30,31], which work in the many-body regime of partial entanglement, but are limited to strictly harmonic muon–nuclear interactions. These start with a Γ-point DFT phonon calculation in the classical muon site geometry (a muon is a localized defect and thus has no q-space dispersion). The usual assumption that, since muons are lighter than nuclei, muon ZPM is fully adiabatically decoupled from the lattice (yielding 3 highest-frequency normal modes ω_j describing single-particle muon ZPM; see Fig. 2c), corresponds to the weakly-bound (zero entanglement) adiabatic limit described above, but with the additional constraint of a harmonic adiabatic potential V_{eff}. This assumption yields directional ZPE contributions $\text{ZPE}_j = \hbar\omega_j/2$ and directional ZPM delocalization $\Delta x_j = \sqrt{\hbar/(2m_\mu\omega_j)}$. The >40% discrepancy between the harmonic and anharmonic weakly-bound adiabatic values of Δx_L thus obtained (Table 1) hints at a breakdown of the harmonic approximation due to strong anharmonicity (Fig. 2a).

Although the weakly-bound adiabatic limit is exact if $m_\mu \to 0$, it cannot reproduce non-zero muon–nuclear entanglement. In fact, in α–N_2 we see strong hybridization of the L muon normal mode with intra-molecular vibrations of both N_2 molecules in the $[N_2$–μ–$N_2]^+$ complex due to a finite muon mass (Fig. 2c), which implies significant muon–nuclear entanglement[49,50]. This is detected by projecting the top 3 (normalized) phonon normal modes onto pure muon motion, summing the squared norms of the resulting (projected) phonon eigenvectors, and subtracting the value 3, which is expected when muon normal modes do not mix with the lattice modes (i.e., in the weakly-bound limit). This

defines an entanglement witness[33–35] w_1, as $w_1 = 0$ for zero muon–nuclear entanglement (weakly-bound adiabatic limit) and $w_1 < 0$ in the entangled, many-body case. For muons in α–N_2 we obtain $w_1 = -0.14 < 0$. This again suggests that the weakly- (and

possibly also the strongly-) bound adiabatic approximation should fail, as muon–nuclear ZPM is inherently many-body, at least in the harmonic approximation. Were it not for strong anharmonicity, which invalidates the approach, such complex ZPM could still be treated by the full, many-body harmonic method by considering the entire supercell Γ-point phonon spectrum.

Full quantum muon description. Finally, we turn to numerically-exact PIMD for calculating observables from arbitrary muon–nuclear ZPM[1–3], based on discretizing imaginary-time, $T > 0$ path integrals. Unlike approximate methods, PIMD works even in the anharmonic many-body regime with partial muon–nuclear entanglement[51]. Using PIMD we find that the projected muon probability density is unimodal in α–N_2 (Fig. 2a, b), confirming that the muon site is unique even for quantum muons[44], with no signs of quantum tunneling. Thoroughly testing PIMD convergence of observables against simplified toy-model simulations, we confirm that all observables are well converged by $P = 16$–24 PIMD beads (imaginary-time steps), except for muon ZPM delocalization Δx_j, where we can correct for finite-P effects via a careful $P \rightarrow \infty$ extrapolation scheme (see Methods and Figs. S3 and S4). We find that muon Δx_L is large enough (Table 1) that anharmonic effects become significant (Fig. 2a) and harmonic approximations fail. Furthermore, all Δx_j are larger than in the weakly- and strongly-bound adiabatic approximations, implying partial muon–nuclear entanglement and many-body ZPM outside of the scope of single-particle approximations, as already anticipated from L normal mode hybridization (Fig. 2c). To quantify the degree of entanglement we calculate a multivariate Pearson correlation coefficient[52]

$$c_i = \frac{\langle \boldsymbol{\delta x}' \cdot \boldsymbol{\delta r}'_{Ni} \rangle}{\sqrt{\langle |\boldsymbol{\delta x}'|^2 \rangle \langle |\boldsymbol{\delta r}'_{Ni}|^2 \rangle}} \in [-1, 1] \qquad (1)$$

between the centered muon displacement $\boldsymbol{\delta x}' = \boldsymbol{\delta x} - \langle \boldsymbol{\delta x} \rangle$ and the centered displacement $\boldsymbol{\delta r}'_{Ni} = \boldsymbol{\delta r}_{Ni} - \langle \boldsymbol{\delta r}_{Ni} \rangle$ of a nucleus i, via PIMD. The quantity $w_{2i} = -|c_i| \in [-1, 0]$ is a witness of muon–nuclear entanglement[33–35], since $w_{2i} = 0$ for separable (weakly-bound) states (as then $\langle \boldsymbol{\delta x}' \cdot \boldsymbol{\delta r}'_{Ni} \rangle = \langle \boldsymbol{\delta x}' \rangle \cdot \langle \boldsymbol{\delta r}'_{Ni} \rangle = 0$), which means that $w_{2i} < 0$ implies entanglement. On the other hand, in the strongly-bound case (maximal entanglement) with $\boldsymbol{\delta \tilde{r}}_{Ni} \propto \boldsymbol{\delta x}$ we find $|c_i| = 100\%$. In α–N_2 the degree of muon–nuclear entanglement is $c_i \approx 30(4)\%$ with the two nearest nitrogen nuclei, and decays with distance (Fig. 1c). This confirms that muon–nuclear ZPM in α–N_2 is partially entangled and thus inherently many-body. We note that a many-body harmonic approximation calculation[29,50] would yield a similar c_i ($\approx 26\%$) between the muon and the two nearest nitrogen nuclei.

QLCR measurements and NQCC of α–N_2. Detailed knowledge of the many-body muon–nuclear ZPM afforded by PIMD allows
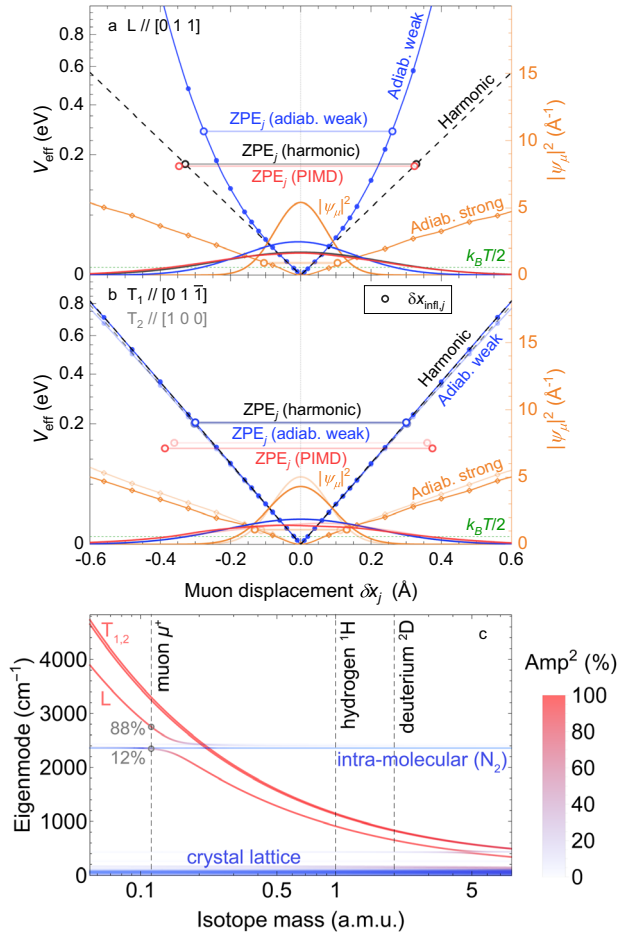

Fig. 2 Effective muon potential and vibrational spectra. Effective muon potential in a square-root-linear scale (harmonic potentials thus appear as straight lines) along the (**a**) L and (**b**) $T_{1,2}$ directions for various approximations (left axis) with the corresponding muon probability density function (right axis), directional zero-point energy (ZPE) contributions ZPE_j, and muon wavefunction inflection points $\delta x_{infl,j}$, where $\partial^2 \psi_\mu / \partial (\delta x_j)^2 = 0$. Under the harmonic approximation, the muon wavefunction width is $\Delta x_j = \delta x_{infl,j}/\sqrt{2}$ (see also Table 1). For path-integral molecular dynamics (PIMD) calculations (at $T = 20$ K), ZPE_j is estimated as the harmonic ZPE_j yielding the same Δx_j if $m_{eff} = m_\mu$ (Table 1). **c** Γ-point phonon spectra of a supercell of muonated α–N_2 vs. muon isotope mass m_μ [plot generated from a single density functional theory (DFT) calculation; see Methods]. Shading corresponds to the muon amplitude squared in individual normal modes.

Table 1 Muon zero-point motion parameters in α-N_2.

Approximation	ZPE (eV)	ZPE_j (eV)	Δx_j (Å)	$m_{eff,j}/m_\mu$
Adiabatic (weakly-bound)	0.69	[0.29, 0.20, 0.20]	[0.16, 0.21, 0.21]	1
Adiabatic (strongly-bound)	0.008(4)	[0.0021, 0.0031, 0.0028]	[0.074(4), 0.093(3), 0.079(4)]	[810(160), 350(40), 520(80)]
Harmonic (weakly-bound)	0.58	[0.17, 0.20, 0.20]	[0.23, 0.21, 0.21]	1
PIMD	0.43(11)*	[0.16(11), 0.13(1), 0.14(1)]*	[0.24(8), 0.27(1), 0.25(1)]	1*

Total muon zero-point energy (ZPE) with directional contributions ZPE_j, muon wavefunction widths Δx_j, and effective muon mass renormalization $m_{eff,j}/m_\mu$ along the $j = $ L, T_1, and T_2 directions, in this order, for the approximations described in the text. Path-integral molecular dynamics (PIMD) ZPE_j was estimated as the harmonic ZPE_j yielding the same Δx_j if $m_{eff} = m_\mu$ is assumed (marked with *).

Table 2 Quadrupolar coupling constant of α-N$_2$.

| Calibration	T (K)	f_{cal}	C_Q^0 (MHz)	Discrepancy (σ)
None		1	−5.76	−7.4(2)
Classical μ^+	1.8	1.106(7)	−5.21(3)	3.1(6)
	5	1.103(4)	−5.22(2)	3.2(7)
Quantum μ^+	1.8	1.076(6)	−5.35(3)	0.7(1)
	5	1.073(4)	−5.37(2)	0.4(1)

Static nuclear quadrupolar coupling constant (NQCC) C_Q^0 of ^{14}N in α-N$_2$ from uncalibrated density functional theory (DFT) calculations, and from calculations calibrated by f_{cal} obtained from fits of experimental quadrupolar level-crossing resonance (QLCR) spectra with predictions for a classical (density functional theory, DFT) or a quantum muon (path-integral molecular dynamics, PIMD; see Fig. 3). Discrepancy from the literature value −5.39(5) MHz[40] is given in standard deviations σ.

us to derive an important constant: the static NQCC of ^{14}N in α-N$_2$, defined as $C_Q^0 = e_0^2 q_0 Q / h$, where $Q = 2.044(3)$ fm^2 is the quadrupolar moment of ^{14}N[42,53], and q_0 is the largest eigenvalue of the electric field gradient (EFG) tensor at the ^{14}N position, assuming static classical nitrogen nuclei. The experimental NQCC at $T = 0$, $C_Q = f(0)C_Q^0$, is reduced from the static C_Q^0 by the solid-nitrogen order parameter $f(0) = 0.863(8) < 1$ due to the ZPM of nitrogen nuclei[40]. Using DFT we calculate C_Q^0 by assuming classical point-particle nuclei in pristine α-N$_2$, obtaining the ab initio value $C_Q^{0,\text{DFT}} = -5.76$ MHz, which differs from the accepted experimental value $C_Q^0 = -5.39(5)$ MHz by $\approx 6.9\%$, or ≈ 7.4 standard deviations σ (Table 2). The discrepancy arises from systematic errors in DFT calculations of EFGs, which are apparently overestimated by a factor $f_{cal} = C_Q^{0,\text{DFT}}/C_Q^0 \approx 1.07(1)$. To obtain an independent estimate of $C_Q^0 = f_{cal}^{-1} C_Q^{0,\text{DFT}}$ we therefore need to determine f_{cal}, and calibrate our ab initio results against experiment.

To achieve this we performed precision QLCR μSR measurements on α-N$_2$. In a QLCR experiment muons stop near $I \geq 1$ nuclei (here ^{14}N), while a longitudinal magnetic field B is swept in small steps at a given T and the muon polarization $P_z(t)$ is measured. For B where the Zeeman splitting of muon spin energy levels approaches the splitting of nuclear energy levels due to EFGs at nuclear positions, resonant cross-relaxation of muon–nuclear spins occurs, resulting in a sharp dip of the measured late-time $P_z(t)$[37–39]. If we also have a good description of muon–nuclear ZPM (e.g., via PIMD), which shifts and reshapes QLCR spectra $P_z(t, B)$, we can extract muonated-sample EFGs and compare them to ab initio DFT predictions of them to find the sought after DFT calibration factor f_{cal}. Since our modeling showed strongly time-window-dependent widths of QLCR spectral peaks in α-N$_2$ (Fig. 3b), we went beyond conventional integral or differential QLCR analysis[39], and performed a simultaneous fit to our data over all measured B and $t < 18$ μs (no binning with a 16 ns time resolution), at each measured T, using a simple global model

$$P_z(t, B) = A_Q P_z^Q(t, B) + A_{\text{Mu}} e^{-\lambda_{\text{Mu}} t} + A_{\text{bgd}}(B) \qquad (2)$$

where A_Q is the amplitude of QLCR signal, P_z^Q is the ab initio-simulated QLCR signal (for either the classical or the quantum case; see Methods) at a given f_{cal}, which was a fit parameter (Fig. 3a, b, and Supplementary Fig. 6), while A_{Mu} describes the muonium fraction, known to form in α-N$_2$[48] and relaxing with rate λ_{Mu}. The contribution $A_{\text{bgd}}(B)$ due to muons stopped outside the sample was modeled as a constant plus a weak Lorentzian of B, with fits yielding a field variation of <10% of the QLCR signal (Fig. 3c), which does not affect our conclusions. These fits described >28,000 experimental data points at each T using only 8 global fit parameters (Fig. 3c, d), with good fit quality (see
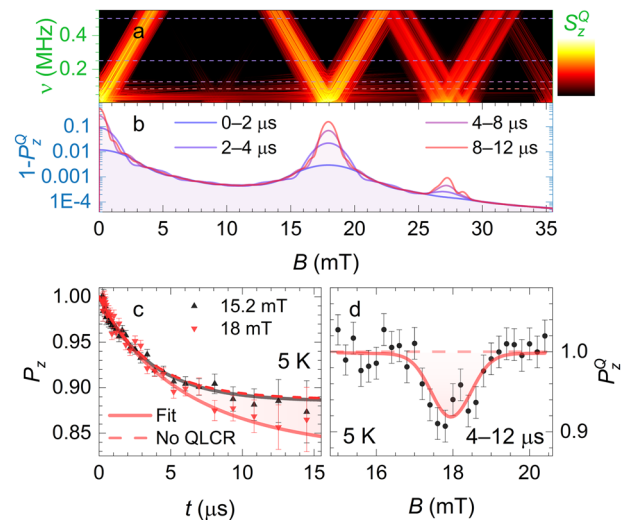
Fig. 3 Muon quadrupolar level-crossing resonance spectra and fits. **a** Calibrated Fourier-transformed quadrupolar level-crossing resonance (QLCR) spectra $S_z^Q(\nu, B)$ vs. frequency ν from path-integral molecular dynamics (PIMD) calculations with 24 beads (see Methods) for time-differential QLCR analysis[39]. **b** Muon-lifetime weighed integrals of $1 - P_z^Q(t, B)$ over different time windows for integral QLCR analysis. **c** Experimental QLCR data at 5 K on (18 mT) and off resonance (15.2 mT) and the global fit with (solid) and without the QLCR term (dashed). **d** Global fit of 5 K QLCR data with PIMD predictions integrated over a 4–12 μs time window vs. B. Error bars on (**c**) and (**d**) represent a statistical uncertainty of one standard deviation.

Methods) and without systematic deviations at any t or B (Supplementary Fig. 5). This held true for both classical and quantum cases, as the main effect of muon–nuclear ZPM was a simple shift of the main QLCR peak, which was absorbed into the fitted value of f_{cal}. Extracting f_{cal} from fits of QLCR spectra under the classical muon ansatz we thus obtain $C_Q^0 = f_{cal}^{-1} C_Q^{0,\text{DFT}} = -5.22(2)$ MHz, which still differs from the accepted experimental value by $\approx 3.2\sigma$ (Table 2). However, extracting f_{cal} from fits of QLCR spectra using a PIMD description of muon–nuclear ZPM, which is well-converged without the need for finite-P extrapolation (see Methods and Supplementary Fig. 3), we obtain excellent agreement with previous experiments, with the final value $C_Q^0 = -5.36(2)$ MHz (Table 2) statistically even more accurate than the previous best estimate of $-5.39(5)$ MHz[40].

Discussion

Based on the above analysis we are able to propose several rules of thumb for when to expect quantum muon effects, which have the potential to significantly impact the interpretation of μSR experiments. Many-body quantum muon effects are expected to be large whenever: (i) the muon is strongly (chemically) bound to the crystal lattice (see Toy model), e.g., when the material is ionic or contains very electronegative atoms, like F$^-$, Cl$^-$, Br$^-$, O^{2-}, or N^{3-}, or functional groups, like OH$^-$, that strongly attract the muon, or (ii) when the phonon normal modes of the pristine material are high-frequency, allowing them to hybridize with, typically high-frequency, muon normal modes (Fig. 2c). For example, the latter scenario is expected when the local chemical bonds in the material around the muon site are strong, e.g., ionic or strong covalent (e.g., double or triple) bonds, or when the material contains light atoms; especially if the bonds are weaker further away from the muon site, for example in molecular crystals, as discussed in the Toy model section. Under the same conditions, muon ZPE is expected to be high, which could

strongly affect the energy ordering, and thus the expected occupancy, of candidate muon sites. These same conditions are also expected to lead to strong deformations of the crystal structure around the muon sites, which suggests a simple rule: if the muon strongly perturbs the crystal structure classically, it likely also becomes quantum entangled with it with a high ZPE. On the other hand, anharmonic quantum muon effects are expected to be important when: (i) the muon is highly delocalized, which occurs when it is weakly bound to neighboring atoms, e.g., at interstitial sites, or, alternatively, (ii) if the effective muon potential is inherently highly anharmonic (Fig. 2a). Muon delocalization and anharmonicity can strongly affect the interpretation of μSR results, since they directly affect the nature and strength of the coupling of the muon to the local magnetic fields. When either just many-body or anharmonic effects are present, they can be treated using appropriate harmonic or adiabatic approximations, respectively. However, as seen in the case of muons in α–N_2, many-body and anharmonic effects can also be present at the same time requiring their careful examination using more general quantum methods. Examples of these include numerically-exact methods like PIMD or the recently-proposed many-interacting-worlds approach[54,55]. We note that the discussion above is independent of the local symmetry, or any lack thereof, at the muon site.

Beyond muons, our unified description of light-particle ZPM, where quantum regimes with well-defined approximations arise in certain limits of particle–lattice entanglement and anharmonicity, directly applies also to other light particles and light-atom nuclei, e.g., hydrogen and lithium, in solids. Such an extension is of immense interest, as nuclear quantum effects were shown to play a crucial role, for example, in stabilizing recent record high-T_c hydride superconductors H_3S[4,56,57] and LaH_{10}[5,58,59], as well as the contentious supposed room-temperature superconductors $LuH_{3-\delta}N_\epsilon$[6,7] and CSH_8[8–10,60], and in explaining their huge isotope effects, as calculated via the self-consistent harmonic approximation[56,57,59]. A similar situation arises in the recent record-density hydrogen storage material $(CH_4)_3(H_2)_{25}$[11], which was found to be stabilized by nuclear quantum effects via the harmonic approximation, and in calculating solvation free energies of Li and F[12] via the quasi-harmonic approximation. In all of these materials, a careful examination of the underlying entanglement and anharmonicity regimes of nuclear ZPM using the approaches described in this paper could reveal any possible limitations on the validity of the approximations used and provide a systematic way of finding even more accurate nuclear ZPM descriptions. In this way, our understanding of these highly intriguing quantum materials could be substantially improved.

In conclusion, we have performed an analysis of muon–nuclear ZPM in α–N_2, culminating in a precision determination of the static NQCC of ^{14}N in pristine α–N_2 using complementary QLCR experiments and state-of-the-art ab initio DFT+PIMD calculations, significantly improving the accuracy of this constant over the previously known value. We also discovered an electric-dipole polaron with strong effective mass renormalization around muons in α–N_2, which might affect the interpretation of experiments purportedly showing quantum tunneling of muonium in this material[23]. In fact, a similar polaron might generically be expected in molecular crystals with charged impurities. More broadly, our work demonstrates the need to consider quantum effects when interpreting μSR data, paying attention to the presence of muon–nuclear entanglement and anharmonicity, to guide the choice of the applicable ZPM approximation. This unified perspective on light-particle ZPM is generally applicable and should be explored further also in the context of material science and quantum chemistry, where it promises to offer a way of finding accurate and computationally-efficient descriptions of

nuclear quantum effects of light atoms across a wide range of quantum materials.

Methods

DFT calculations. Both the pristine and muonated low-T low-pressure α phase of solid nitrogen, α–N_2, was studied using the CASTEP plane-wave ab initio density functional theory (DFT) code[61] using the PBE exchange–correlation functional[62] and ultrasoft pseudopotentials. Calculations were carried out on a $2 \times 2 \times 2$ supercell to avoid finite-size effects around the implanted muon, while a 1200 eV plane-wave energy cutoff and $2 \times 2 \times 2$ Monkhorst–Pack grid[63] reciprocal-space sampling was chosen to achieve numerical convergence. A neutral cell was used for pristine structure calculations, while a positive elementary charge per supercell was applied in calculations of muonated structures, to account for the positive charge of the muon. All calculations were converged to within a total energy tolerance of 0.1 neV/atom in the self-consistent field (SCF) DFT loop, while geometry relaxation tasks were converged to within a tight 5 meV Å^{-1} force tolerance on the muon and nuclei. Furthermore, to properly account for weak cohesive van der Waals (VdW) dispersion forces between N_2 molecules, which are usually underestimated in pure DFT, a Tkatchenko–Scheffler (TS) semi-empirical dispersion correction scheme was applied in a DFT-D approach[64]. We note, though, that the results of ordinary DFT with an ad hoc isotropic external hydrostatic pressure of 0.5 GPa (chosen to reproduce the experimental zero-pressure unit cell volume of pristine α–N_2) were practically indistinguishable from the results of full DFT-D calculations, even in the presence of an implanted muon. This indicates that in α–N_2 the dominant VdW dispersion force contribution is a simple isotropic attraction among all nuclei and the muon.

Despite competing suggestions of a $Pa\bar{3}$ (No. 205) or a $P2_13$ (No. 198) cubic crystallographic structure of pristine α–N_2 in the literature[40], we find that the higher-symmetry $Pa\bar{3}$ structure is moderately preferred in our DFT calculations (by ~ 0.05 eV per unit cell), in line with recent consensus[41,42,65]. In this structure the centers of N_2 molecules form a face-centered cubic lattice (Supplementary Fig. 1a).

Classical muon stopping site. To find candidate muon stopping sites in α–N_2 a muon's initial position was randomly seeded in the unit cell and the full crystal geometry (including the muon position) relaxed at a fixed, experimental cell volume until convergence. This process was repeated >20 times to generate a list of candidate muon stopping sites, which were then grouped into clusters by identifying those candidate muon sites within <0.7 Å of each other (or of any in-between sites) as belonging to the same cluster. Here the distance between two arbitrary candidate muon sites $\mathbf{r}_{\mu 1}$ and $\mathbf{r}_{\mu 2}$ was taken as the minimal possible real-space distance $|\mathbf{r}_{\mu 1} - T\mathbf{r}_{\mu 2}|$ under any symmetry operation T in the pristine α–N_2 crystallographic space group $Pa\bar{3}$ (including discrete translational, rotational and reflection symmetries). This is because the implanted muon is the sole source of local symmetry breaking in the crystal and thus muon sites related by pristine space-group symmetry operations should be regarded as identical. A muon site cluster can thus be thought of as a connected component in a graph whose vertices are the calculated muon sites that are considered adjacent if their minimal, symmetry-reduced distance is below a chosen threshold (0.7 Å in our case). We note that this symmetry-aware clustering algorithm based on graph theory is also implemented in the user-friendly MuFinder program for determining and analysing muon stopping sites[19,25]. In the end, we find a single muon site cluster in α–N_2, which lies at the point midway between the centers of the two neighboring N_2 molecules of the pristine α–N_2 structure (Supplementary Fig. 1b).

Γ-point phonon spectra were calculated on a $2 \times 2 \times 2$ supercell of α–N_2, with the whole isotope effect plot (Fig. 2c) generated from a single DFT calculation of phonon normal modes and frequencies. This was achieved by first reconstructing the dynamical matrix (DM)[49,50] of the muonated crystal, reweighting it by the desired muon isotope mass m_μ, and then rediagonalizing it to obtain the new phonon normal modes and frequencies.

Choice of the exchange–correlation functional. We note that switching to an a priori less accurate local density approximation (LDA) DFT exchange–correlation functional[61] does not significantly alter our results. Namely, the classical muon–nuclear distance in the $[N_2-\mu-N_2]^+$ complex changes by just −0.01 Å, the total harmonic ZPE of the 3 highest-frequency (muon) normal modes changes by +4.1% compared to the PBE functional, and the harmonic (under)estimate of the entanglement coefficient c_i of the muon with the two nearest nitrogen nuclei changes from ≈26% to ≈24%. The anharmonicity measure $V_{\text{eff}}^{\text{weak}}(2\delta\mathbf{x})/(4V_{\text{eff}}^{\text{weak}}(\delta\mathbf{x}))$, which would equal 1 for a purely harmonic potential, at a typical displacement $2\delta x = +0.24$ Å along the most anharmonic direction L (Fig. 2a) changes slightly, from 1.8 to 1.6, when switching from PBE to LDA. Many-body and anharmonic ZPM effects of muons in α–N_2 are thus rather robust against the choice of the exchange–correlation functional. Nevertheless, we used PBE for all the results reported in the manuscript, as described above, since it is in general expected to be much more accurate than LDA for describing electronic systems, such as α–N_2, where electrons are not highly correlated.

Classical MD and quantum PIMD calculations. For PIMD calculations an NVT statistical ensemble of up to $P = 32$ beads was simulated for up to $S = 8600$ steps of 0.5 fs with a $T = 20$ K stochastic Langevin thermostat. Satisfactory convergence in bead number was achieved already for $P = 16$–24 beads for all QLCR resonance parameters (Supplementary Fig. 3) and positional observables (Supplementary Fig. 4) except for the muon wavefunction widths (Supplementary Fig. 4a), which had to be extrapolated to the $P \to \infty$ limit (see heading Extrapolation of PIMD muon widths). Classical MD simulations (which can be interpreted as $P = 1$ PIMD simulations) used the same statistical ensemble, time step, temperature, and thermostat and were run for up to $S = 12{,}000$ steps. Care was taken to ensure proper thermalization of the ensembles before observables were extracted from them.

Both PIMD and MD simulations produce a list of SP muon–nuclear configurations $\{\mathbf{r}_i^{(s,p)}\}_{i=1}^{K}$, where $s = 1, ..., S$ is the time step, $p = 1, ..., P$ is the bead index, and $\mathbf{r}_i$ is the position of one muon or nucleus i out of K muons and nuclei present in the system. These muon–nuclear configurations follow the corresponding Boltzmann statistical probability distribution for finding muons and nuclei at these positions. In the case of MD this is the $T > 0$ classical thermal probability distribution $\rho_c(\mathbf{r}_1, ..., \mathbf{r}_K)$, while in PIMD this is the quantum thermal probability distribution $\rho_q(\mathbf{r}_1, ..., \mathbf{r}_K)$, which at $T = 0$ would coincide with the ground-state wavefunction's $|\psi\rangle$ probability distribution $\rho_q(\mathbf{r}_1, ..., \mathbf{r}_K) = |\psi(\mathbf{r}_1, ..., \mathbf{r}_K)|^2$. The thermal expectation value $\langle O \rangle$ of any observable O that depends only on muon–nuclear positions can thus be approximated from numerical PIMD or MD samples by calculating the average

$$\langle O \rangle \approx \frac{1}{SP} \sum_{s=1}^{S} \sum_{p=1}^{P} O(\mathbf{r}_1^{(s,p)}, ..., \mathbf{r}_K^{(s,p)}) \qquad (3)$$

For observables that were expensive to calculate [e.g., the electric field gradients (EFG), which require a full DFT calculation for each muon–nuclear configuration in the above average] a further Monte Carlo approximation to the average was employed by randomly sampling only a small number of s and p (≈ 120 in the case of EFGs) in Eq. (3). For certain numerically-noisy observables, like the directional wavefunction widths in Table 1, multiple runs at a given P were merged together to improve statistics and provide a more reliable numerical estimate.

ZPM and quantum entanglement from PIMD. A numerical estimate of the average position $\langle \mathbf{r}_i \rangle$ of a given muon or nucleus i can be calculated in this way by choosing $O(\mathbf{r}_1, ..., \mathbf{r}_K) = \mathbf{r}_i$ in Eq. (3). From this we can estimate the squared gyration radius $\Delta r_i^2 = \langle |\delta \mathbf{r}_i|^2 \rangle = \langle |\mathbf{r}_i - \langle \mathbf{r}_i \rangle|^2 \rangle$, which corresponds to choosing $O = |\mathbf{r}_i - \langle \mathbf{r}_i \rangle|^2$, and the covariance $\langle \delta \mathbf{r}_i \cdot \delta \mathbf{r}_{i'} \rangle$ by choosing $O = (\mathbf{r}_i - \langle \mathbf{r}_i \rangle) \cdot (\mathbf{r}_{i'} - \langle \mathbf{r}_{i'} \rangle)$. Using these we can then extract a numerical estimate of the multivariate Pearson correlation coefficient $c_{ii'} = \langle \delta \mathbf{r}_i \cdot \delta \mathbf{r}_{i'} \rangle / (\Delta r_i \Delta r_{i'}) \in [-1, 1]$[52], as in Eq. (1). If this is non-zero at $T \to 0$ it implies ground-state positional entanglement of muons or nuclei i and i' (see Results). We can also calculate the squared ZPM delocalization of a muon Δx_j^2 along a given direction $j = \mathrm{L}, \mathrm{T}_1, \mathrm{T}_2$, by choosing $O = |(\boldsymbol{\delta x} - \langle \boldsymbol{\delta x} \rangle) \cdot \hat{\mathbf{v}}_j|^2$, where $\boldsymbol{\delta x}$ is the muon displacement, for the corresponding unit vector $\hat{\mathbf{v}}_j$ along the direction j.

Extrapolation of PIMD muon widths. While the covariance of muon–nuclear positions (Supplementary Fig. 4b), the wavefunction widths of the nitrogen nuclei (Supplementary Fig. 4c), and QLCR resonance parameters (Supplementary Fig. 3) all fully converge for $P = 16$–24 beads, the muon wavefunction widths Δx_j do not (Supplementary Fig. 4a). However, numerical estimates of expected PIMD convergence under the harmonic toy model described in the main text indicate that the muon wavefunction width is expected to be underestimated by the same factor of $g \approx 0.55(2)$ at $P = 24$ compared to the $P \to \infty$ limit in all three directions j (Supplementary Fig. 4a). This allows us to estimate the true values of Δx_j in the $P \to \infty$ limit (Table 1) by dividing the raw PIMD values $\Delta x_j = 0.13, 0.15,$ and 0.14 Å along the L, T_1, and T_2 directions, respectively, by this factor g. Moreover, as these widths feature in the multivariate Pearson correlation coefficient c_i in Eq. (1), we estimate the true values of this entanglement proxy c_i in the $P \to \infty$ limit (Fig. 1c) by multiplying raw PIMD values by the same factor g.

As this procedure mostly neglects anharmonic effects, which are relevant along the $j = \mathrm{L}$ direction, we estimate the additional relative systematic uncertainty due to this omission along the direction $j = \mathrm{L}$ from the relative difference of Δx_j values in the anharmonic weakly-bound adiabatic approximation and the harmonic approximation (Table 1), as a proxy for the influence of anharmonic effects. This yields an additional relative systematic uncertainty of at most $\approx 30\%$ in the muon wavefunction width along the $j = \mathrm{L}$ direction, and $\approx 10\%$ in the entanglement witness c_i.

Finally, we note the robustness of this extrapolation scheme, as even the harmonic weakly-bound adiabatic approximation (corresponding to $N = 0$ dynamical nuclei around the muon in the toy model), which is expected to be much less accurate than the $N = 2$ toy model for estimating PIMD convergence, yields a similar estimate of $g \approx 0.47(2)$ at $P = 24$.

Thermal effects and classical MD. Since PIMD calculations require a finite temperature for numerical convergence ($T = 20$ K in our calculations) we also checked

that the observed quantum effects were not masked by thermal excitations by comparing quantum PIMD calculations against complementary classical MD simulations at the same T. We find that the classical thermal spread of muon–nuclear positions is indeed predicted to be much smaller than the quantum wavefunction widths (Table 1), giving just $\Delta x_j = 0.08$ and 0.07 Å along $j = \mathrm{L}$ and $\mathrm{T}_{1,2}$, respectively, as can be expected from the steepness of the calculated adiabatic and harmonic effective potentials (Fig. 2a, b) in relation to the thermal equipartition energy $k_B T/2 = 1.7$ meV at this T, where k_B is the Boltzmann constant.

Furthermore, quantum-mechanically a transition from T-independent ground-state ZPM to thermally-excited, T-dependent quantum behavior along a given direction j upon increasing T is only expected when $k_B T$ becomes comparable to the splitting ΔE_j between the ground-state and the first excited ZPM state. Namely, when $k_B T \ll \Delta E_j$ the system is effectively frozen in its quantum ground state, in contrast to the classical point-particle prediction of a T-dependent spread of muon–nuclear positions down to the lowest T. Under the harmonic approximation this splitting can be obtained as $\Delta E_j = 2\mathrm{ZPE}_j$, while $\Delta E_j > 2\mathrm{ZPE}_j$ when anharmonicity that increases the effective potential at larger displacements is present, as, e.g., in the case of muons in α-N_2 along the $j = \mathrm{L}$ direction (Fig. 2a). From Table 1 we can see that all considered approximations point to muons in α-N_2 being in the low-T, $k_B T \ll \Delta E_j$ regime along all directions j at the considered temperatures. We thus conclude that thermal effects are irrelevant for muon ZPM in α-N_2 at these low T, and that the muon–nuclear system is, in fact, in its T-independent quantum ground state, at least locally around the muon.

QLCR spectra calculations. If we were to assume fixed classical muon–nuclear positions $\{\mathbf{r}_i\}_{i=1}^{K}$ and the corresponding EFG tensors $\{V_i\}_{i=1}^{K}$ at those positions (these can be calculated from the muon–nuclear positions using DFT), the muon and nuclear spins would interact via a Hamiltonian H composed of a Zeeman contribution H_Z, a local quadrupolar contribution H_Q, and a dipole coupling contribution H_D[37,38,66,67]

$$\begin{aligned} H &= & H_Z + H_Q + H_D \\ H_Z &= & -\sum_i \gamma_i \hbar \mathbf{S}_i \cdot \mathbf{B} \\ H_Q &= & \sum_i \frac{e_0 Q_i}{2 S_i (2 S_i - 1)} \mathbf{S}_i \cdot V_i \mathbf{S}_i \\ H_D &= & \sum_{\langle ii' \rangle} \frac{\mu_0 \gamma_i \gamma_{i'} \hbar^2}{4\pi |\mathbf{r}_{ii'}|^3} \left[\mathbf{S}_i \cdot \mathbf{S}_{i'} - 3(\mathbf{S}_i \cdot \hat{\mathbf{r}}_{ii'})(\hat{\mathbf{r}}_{ii'} \cdot \mathbf{S}_{i'}) \right] \end{aligned} \qquad (4)$$

where γ_i is the gyromagnetic ratio of muon or nucleus i with spin vector $\mathbf{S}_i$, spin size S_i, and nuclear quadrupole moment Q_i, $\mathbf{B}$ is the applied magnetic field, e_0 is the elementary charge, μ_0 is vacuum permeability, the sum in H_D is over unique pairs of muon or nuclei $\langle ii' \rangle$, $\mathbf{r}_{ii'} = \mathbf{r}_i - \mathbf{r}_{i'}$ is a vector from a muon or nucleus i' to i, and $\hat{\mathbf{r}}_{ii'} = \mathbf{r}_{ii'}/|\mathbf{r}_{ii'}|$ is a unit vector in the same direction. However, due to both quantum ZPM and thermal movement the muons and nuclei described by this Hamiltonian do not have fixed classical (point-particle) positions, nor are the EFGs independent of those positions.

To reduce the complexity of solving the full, coupled spin–positional Hamiltonian of Eq. (4), we assume that there is no significant entanglement between the spin and spatial degrees of freedom in the $T \approx 0$ ground-state wavefunction of the system, i.e., that $|\psi\rangle = |\psi\rangle_{\mathrm{spin}} \otimes |\psi\rangle_{\mathrm{position}}$, due to a separation of timescales for positional and spin dynamics. In this way we can construct an effective spin-only Hamiltonian operator by averaging out the positional degrees of freedom with a partial trace

$$H_{\mathrm{eff,spin}} = \mathrm{tr}_{\mathrm{position}} \{ \rho H \} \qquad (5)$$

where ρ is the total density matrix, which at $T = 0$ equals simply $\rho = |\psi\rangle\langle\psi|$; i.e., at $T = 0$ we have $H_{\mathrm{eff,spin}} = _{\mathrm{position}}\langle\psi|H|\psi\rangle_{\mathrm{position}}$. In PIMD and MD simulations this can be done numerically by calculating an average over positional degrees of freedom via Eq. (3) where the observable O is taken to be the full Hamiltonian H from Eq. (4), and at each muon–nuclear configuration sample $\{\mathbf{r}_i^{(s,p)}\}_{i=1}^{K}$ we recalculate the corresponding EFG tensors V_i via DFT. As mentioned previously, due to the time complexity of calculating the EFG tensors, the full average in Eq. (3) is approximated via Monte Carlo sampling of ≈ 120 random s and p indices from the PIMD or MD muon–nuclear configurations $\{\mathbf{r}_i^{(s,p)}\}_{i=1}^{K}$.

The numerical calculation of a single Hamiltonian sample [Eq. (4)] from the muon–nuclear configuration and the corresponding EFG tensors was performed using the CalcALC program[68,69] by considering only the four $^{14}\mathrm{N}$ nuclei in the $[\mathrm{N}_2\text{-}\mu\text{-}\mathrm{N}_2]^+$ complex, i.e., the four nitrogen nuclei closest to the muon, since further-away nitrogen nuclei are only very weakly dipolarly coupled to the muon and thus do not affect its relaxation much. A $^{14}\mathrm{N}$ nuclear quadrupole moment of $Q = 2.044(3)$ fm^2 was used[42,53]. Once the effective spin-only Hamiltonian [Eq. (5)] was thus calculated via Eq. (3), a CalcALC-inspired Python program was used to calculate the time-dependent muon relaxation signal $P_z^Q(t)$ due to QLCR via exact diagonalization, as in Ref. [70], for a range of applied magnetic fields B. At this stage, the quadrupolar contribution H_Q was multiplied by an EFG calibration factor $f_{\mathrm{cal}}^{-1} \approx 1$, removing most of the otherwise unavoidable systematic errors of DFT (see the Results section). In global fits of experimental QLCR spectra f_{cal} was adjusted in a loop until convergence to a minimal χ^2 was achieved. We note that in

these fits no systematic deviations at any t or B were observed (Supplementary Fig. 5). The total global fit quality was $\chi^2/\text{DOF} = 1.06$ and 1.08 at $T = 1.8$ and 5 K, respectively.

The final, calibrated QLCR spectra $1 - P_z^Q(t, B)$ exhibit a non-trivial dependence on time t and applied field B and are shown in Supplementary Fig. 6. Figure 3a shows their Fourier transforms

$$S_z^Q(\nu, B) = \frac{1}{2\pi} \int_{-\infty}^{\infty} \left[1 - P_z^Q(t, B)\right] e^{-2\pi i \nu t} \, dt \qquad (6)$$

under the convention $P_z^Q(-t, B) = P_z^Q(t, B)$ and where ν is the frequency, while Fig. 3b shows their weighed time integrals

$$\overline{P}_z^Q(B) = \frac{\int_{t_1}^{t_2} P_z^Q(t, B) e^{-t/\tau_\mu} \, dt}{\int_{t_1}^{t_2} e^{-t/\tau_\mu} \, dt} \qquad (7)$$

over select time windows $t \in [t_1, t_2]$, weighed by the mean muon lifetime $\tau_\mu = 2.197 \, \mu s$[71] to account for the exponential decay of muons and their subsequent Poissonian counting statistics in μSR measurements[15].

QLCR measurements. QLCR μSR measurements on α–N_2 were performed on the EMU beamline[72] (ISIS pulsed muon source), using a custom-built TiZr gas condensation cell. A 100 μm thick Ti window allowed surface muons to enter the sample volume, while a separate experiment confirmed negligible muon depolarisation in TiZr over the studied T. A ^{4}He exchange gas cryostat around the cell provided control over sample T down to ~1.5 K, while a 1/8" capillary connecting the cell to an external gas supply was heated along its length to avoid blockages. The sample was condensed from high purity (Grade 6.0) N_2 gas, with $\approx$1.8 bar L^{-1} of gas being condensed at $\approx$65 K to ensure the $\approx$1.6 cm^3 sample volume was full. Gas pressure was maintained well above the N_2 triple point ($\approx$0.125 bar) throughout sample condensation to avoid deposition of the gas directly into the solid phase. Once condensation was complete, the sample was cooled through the freezing point at $\approx$0.6 K/min, with the form of μSR spectra recorded at 58 K (β–N_2 phase) compared to earlier data on this system[48], as well as our higher-T data, to confirm the sample was frozen.

Data availability
The data presented in this paper[73] are available at https://doi.org/10.6084/m9.figshare.23203037. All other data are available from the corresponding author on reasonable request. Supplementary Movies 1 and 2 present animated versions of Fig. 1a and b, respectively.

Code availability
The computer code used to generate and/or analyse the data in this paper[73] is available at https://doi.org/10.6084/m9.figshare.23203037.

References
1. Herrero, C. P. & Ramírez, R. Path-integral simulation of solids. *J. Phys. Condens. Matter.* **26**, 233201 (2014).
2. Ceriotti, M. et al. Nuclear quantum effects in water and aqueous systems: Experiment, theory, and current challenges. *Chem. Rev.* **116**, 7529–7550 (2016).
3. Markland, T. E. & Ceriotti, M. Nuclear quantum effects enter the mainstream. *Nat. Rev. Chem.* **2**, 1–14 (2018).
4. Drozdov, A., Eremets, M., Troyan, I., Ksenofontov, V. & Shylin, S. I. Conventional superconductivity at 203 kelvin at high pressures in the sulfur hydride system. *Nature* **525**, 73–76 (2015).
5. Drozdov, A. et al. Superconductivity at 250 K in lanthanum hydride under high pressures. *Nature* **569**, 528–531 (2019).
6. Dasenbrock-Gammon, N. et al. Evidence of near-ambient superconductivity in a N-doped lutetium hydride. *Nature* **615**, 244–250 (2023).
7. Ming, X. et al. Absence of near-ambient superconductivity in LuH$_{2+x}$N$_y$. *Nature* (2023).
8. Snider, E. et al. Room-temperature superconductivity in a carbonaceous sulfur hydride. *Nature* **586**, 373–377 (2020).
9. Snider, E. et al. Retraction note: Room-temperature superconductivity in a carbonaceous sulfur hydride. *Nature* **610**, 804 (2022).
10. Eremets, M. et al. High-temperature superconductivity in hydrides: experimental evidence and details. *J. Supercond. Nov. Magn.* **35**, 965 (2022).
11. Ranieri, U. et al. Formation and stability of dense methane-hydrogen compounds. *Phys. Rev. Lett.* **128**, 215702 (2022).
12. Duignan, T. T., Baer, M. D., Schenter, G. K. & Mundy, C. J. Real single ion solvation free energies with quantum mechanical simulation. *Chem. Sci.* **8**, 6131–6140 (2017).
13. Ackland, G. J. et al. Quantum and isotope effects in lithium metal. *Science* **356**, 1254–1259 (2017).
14. Blundell, S. J. Spin-polarized muons in condensed matter physics. *Contemp. Phys.* **40**, 175–192 (1999).
15. Blundell, S. J., De Renzi, R., Lancaster, T. & Pratt, F. L. *Muon Spectroscopy: An Introduction*. (Oxford University Press, Oxford, 2021).
16. Yaouanc, A. & De Réotier, P. D. *Muon spin rotation, relaxation, and resonance: applications to condensed matter*. (Oxford University Press, Oxford, 2011).
17. Möller, J. S. et al. Playing quantum hide-and-seek with the muon: localizing muon stopping sites. *Phys. Scr.* **88**, 068510 (2013).
18. Bonfà, P. & De Renzi, R. Toward the computational prediction of muon sites and interaction parameters. *J. Phys. Soc. Jpn.* **85**, 091014 (2016).
19. Huddart, B. M. Muon stopping sites in magnetic systems from density functional theory. Ph.D. thesis, Durham University, Durham, UK (2020). http://etheses.dur.ac.uk/13423/.
20. Mañas-Valero, S., Huddart, B. M., Lancaster, T., Coronado, E. & Pratt, F. L. Quantum phases and spin liquid properties of 1T-TaS$_2$. *npj Quantum Mater.* **6**, 1–9 (2021).
21. Prando, G. et al. Common effect of chemical and external pressures on the magnetic properties of RCoPO (R = La, Pr). *Phys. Rev. B* **87**, 064401 (2013).
22. Onuorah, I. J. et al. Quantum effects in muon spin spectroscopy within the stochastic self-consistent harmonic approximation. *Phys. Rev. Materials* **3**, 073804 (2019).
23. Storchak, V. G. & Prokof'ev, N. V. Quantum diffusion of muons and muonium atoms in solids. *Rev. Mod. Phys.* **70**, 929–978 (1998).
24. Herrero, C. P. & Ramírez, R. Diffusion of muonium and hydrogen in diamond. *Phys. Rev. Lett.* **99**, 205504 (2007).
25. Huddart, B. et al. Mufinder: A program to determine and analyse muon stopping sites. *Comput. Phys. Commun.* **280**, 108488 (2022).
26. Soudackov, A. V. & Hammes-Schiffer, S. Removal of the double adiabatic approximation for proton-coupled electron transfer reactions in solution. *Chem. Phys. Lett.* **299**, 503–510 (1999).
27. Porter, A. R., Towler, M. D. & Needs, R. J. Muonium as a hydrogen analogue in silicon and germanium: Quantum effects and hyperfine parameters. *Phys. Rev. B* **60**, 13534–13546 (1999).
28. Bonfà, P., Sartori, F. & De Renzi, R. Efficient and reliable strategy for identifying muon sites based on the double adiabatic approximation. *J. Phys. Chem. C* **119**, 4278–4285 (2015).
29. Monacelli, L. et al. The stochastic self-consistent harmonic approximation: calculating vibrational properties of materials with full quantum and anharmonic effects. *J. Phys. Condens. Matter.* **33**, 363001 (2021).
30. Boxwell, M. A., Claxton, T. A. & Cox, S. F. J. Ab initio calculations on the hyperfine isotope effect between C$_{60}$H and C$_{60}$Mu. *J. Chem. Soc., Faraday Trans.* **89**, 2957–2960 (1993).
31. Möller, J. S., Ceresoli, D., Lancaster, T., Marzari, N. & Blundell, S. J. Quantum states of muons in fluorides. *Phys. Rev. B* **87**, 121108(R) (2013).
32. Yamada, K., Kawashima, Y. & Tachikawa, M. Accurate prediction of hyperfine coupling constants in muoniated and hydrogenated ethyl radicals: ab initio path integral simulation study with density functional theory method. *J. Chem. Theory Comput.* **10**, 2005–2015 (2014).
33. Plenio, M. B. & Virmani, S. An introduction to entanglement measures. *Quantum Info. Comput.* **7**, 1–51 (2007).
34. Horodecki, R., Horodecki, P., Horodecki, M. & Horodecki, K. Quantum entanglement. *Rev. Mod. Phys.* **81**, 865–942 (2009).
35. Horodecki, R. Quantum information. *Acta Phys. Pol.* **139**, 197–218 (2021).
36. Claxton, T. A. Muon-nuclear quadrupolar level crossing resonance in solid nitrogen. Evidence for [N$_2$MuN$_2$]$^+$ complex formation? *Philos. Mag. B* **72**, 251–257 (1995).
37. Abragam, A. Spectrométrie par croisements de niveaux en physique du muon. *C. R. Acad. Sci. Ser. B* **229**, 95–99 (1984).
38. Storchak, V. et al. Muon-nuclear quadrupolar level crossing resonance in solid nitrogen. Evidence for N$_2\mu^+$ ion formation. *Chem. Phys. Lett.* **200**, 546–551 (1992).
39. Lord, J. S., Pratt, F. L. & Telling, M. T. F. Time differential ALC – experiments, simulations and benefits. *J. Phys. Conf. Ser.* **551**, 012058 (2014).
40. Scott, T. A. Solid and liquid nitrogen. *Phys. Rep.* **27**, 89–157 (1976).
41. Erba, A., Maschio, L., Salustro, S. & Casassa, S. A post-Hartree–Fock study of pressure-induced phase transitions in solid nitrogen: The case of the α, γ, and ε low-pressure phases. *J. Chem. Phys.* **134**, 074502 (2011).
42. Rumble, J. CRC Handbook of Chemistry and Physics (CRC Press/Taylor & Francis Group, Boca Raton, 2021), 102 edn.
43. Botschwina, P. et al. Theoretical investigations of proton-bound cluster ions. *Faraday Discuss.* **118**, 433–453 (2001).

44. Terrill, K. & Nesbitt, D. J. Ab initio anharmonic vibrational frequency predictions for linear proton-bound complexes OC-H+-CO and N₂-H+-N₂. *Phys. Chem. Chem. Phys.* **12**, 8311–8322 (2010).

45. Yu, Q. et al. Structure, anharmonic vibrational frequencies, and intensities of NNHNN+. *J. Phys. Chem. A* **119**, 11623–11631 (2015).

46. Liao, H.-Y., Tsuge, M., Tan, J. A., Kuo, J.-L. & Lee, Y.-P. Infrared spectra and anharmonic coupling of proton-bound nitrogen dimers N₂–H+–N₂, N₂–D+–N₂, and ¹⁵N₂–H+–¹⁵N₂ in solid para-hydrogen. *Phys. Chem. Chem. Phys.* **19**, 20484–20492 (2017).

47. Hooper, R., Boutwell, D. & Kaledin, M. Assignment of infrared-active combination bands in the vibrational spectra of protonated molecular clusters using driven classical trajectories: Application to N₄H+ and N₄D+. *J. Phys. Chem. A* **123**, 5613–5620 (2019).

48. Storchak, V., Brewer, J. H., Morris, G. D., Arseneau, D. J. & Senba, M. Muonium formation via electron transport in solid nitrogen. *Phys. Rev. B* **59**, 10559–10572 (1999).

49. Srivastava, G. P. *The Physics of Phonons.* (A. Hilger, Bristol Philadelphia, 1990).

50. Kantorovich, L. *Quantum Theory of the Solid State: An Introduction.* (Kluwer Academic Publishers, Dordrecht Boston, 2004).

51. Shiga, M. Path integral simulations. In *Reference Module in Chemistry, Molecular Sciences and Chemical Engineering* (Elsevier, 2018). https://www.sciencedirect.com/science/article/pii/B9780124095472116142.

52. Ichiye, T. & Karplus, M. Collective motions in proteins: A covariance analysis of atomic fluctuations in molecular dynamics and normal mode simulations. *Proteins* **11**, 205–217 (1991).

53. Tokman, M., Sundholm, D., Pyykkö, P. & Olsen, J. The nuclear quadrupole moment of ¹⁴N obtained from finite-element MCHF calculations on N²⁺ (2p; ²P₃/₂) and N⁺ (2p²; ³P₂ and 2p²; ¹D₂). *Chem. Phys. Lett.* **265**, 60–64 (1997).

54. Hall, M. J. W., Deckert, D.-A. & Wiseman, H. M. Quantum phenomena modeled by interactions between many classical worlds. *Phys. Rev. X* **4**, 041013 (2014).

55. Sturniolo, S. Computational applications of the many-interacting-worlds interpretation of quantum mechanics. *Phys. Rev. E* **97**, 053311 (2018).

56. Errea, I. et al. High-pressure hydrogen sulfide from first principles: A strongly anharmonic phonon-mediated superconductor. *Phys. Rev. Lett.* **114**, 157004 (2015).

57. Errea, I. et al. Quantum hydrogen-bond symmetrization in the superconducting hydrogen sulfide system. *Nature* **532**, 81–84 (2016).

58. Somayazulu, M. et al. Evidence for superconductivity above 260 K in lanthanum superhydride at megabar pressures. *Phys. Rev. Lett.* **122**, 027001 (2019).

59. Errea, I. et al. Quantum crystal structure in the 250-kelvin superconducting lanthanum hydride. *Nature* **578**, 66–69 (2020).

60. Hirsch, J. & Marsiglio, F. Unusual width of the superconducting transition in a hydride. *Nature* **596**, E9–E10 (2021).

61. Clark, S. J. et al. First principles methods using CASTEP. *Z. Kristall.* **220**, 567–570 (2005).

62. Perdew, J. P., Burke, K. & Ernzerhof, M. Generalized gradient approximation made simple. *Phys. Rev. Lett.* **77**, 3865–3868 (1996).

63. Monkhorst, H. J. & Pack, J. D. Special points for Brillouin-zone integrations. *Phys. Rev. B* **13**, 5188–5192 (1976).

64. Tkatchenko, A. & Scheffler, M. Accurate molecular Van Der Waals interactions from ground-state electron density and free-atom reference data. *Phys. Rev. Lett.* **102**, 073005 (2009).

65. Maynard-Casely, H. E., Hester, J. R. & Brand, H. E. A. Re-examining the crystal structure behaviour of nitrogen and methane. *IUCrJ* **7**, 844–851 (2020).

66. Ashbrook, S. E. & Duer, M. J. Structural information from quadrupolar nuclei in solid state NMR. *Concepts Magn. Reson. Part A Bridg. Educ. Res.* **28A**, 183–248 (2006).

67. Slichter, C *Principles of Magnetic Resonance.* (Springer: Berlin), 1990.

68. Pratt, F. L. A user tool for predicting and interpreting Muon ALC and QLCR spectra. http://shadow.nd.rl.ac.uk/calcalc/. Accessed: 2021-09-17.

69. Berlie, A., Pratt, F. L., Huddart, B. M., Lancaster, T. & Cottrell, S. P. Muon–nitrogen quadrupolar level crossing resonance in a charge transfer salt. *J. Phys. Chem. C* **126**, 7529–7534 (2022).

70. Lord, J., Cottrell, S. & Williams, W. Muon spin relaxation in strongly coupled systems. *Phys. B Condens. Matter* **289-290**, 495–498 (2000).

71. Zyla, P. et al. Review of Particle Physics. *Prog. Theor. Exp. Phys.* 2020 (2020). https://doi.org/10.1093/ptep/ptaa104. 083C01, https://academic.oup.com/ptep/article-pdf/2020/8/083C01/34673722/ptaa104.pdf.

72. Giblin, S. et al. Optimising a muon spectrometer for measurements at the ISIS pulsed muon source. *Nucl. Instrum. Methods Phys. Res. A* **751**, 70–78 (2014).

73. Data and computer code from this paper can be found at https://doi.org/10.6084/m9.figshare.23203037.

Author contributions

The project was originally conceived by T.L. and F.L.P. M.G. carried out DFT, MD, and PIMD calculations under the supervision of T.L. and S.J.C., and developed the unified description of muon–nuclear entanglement and anharmonicity. F.L.P. and S.P.C. conceived of and set up the QLCR experiments and performed them with assistance from M.G. QLCR data was analyzed by F.L.P., S.P.C., and M.G. with QLCR calculations performed by M.G. and F.L.P. All authors discussed the results. M.G. wrote the paper with feedback from all the authors.

Competing interests

The authors declare no competing interests.

Additional information

Supplementary information The online version contains supplementary material available at https://doi.org/10.1038/s42005-023-01260-7.

Correspondence and requests for materials should be addressed to Matjaž Gomilšek.

Peer review information : *Communications Physics* thanks Lorenzo Monacelli and the other, anonymous, reviewer(s) for their contribution to the peer review of this work. A peer review file is available.

Reprints and permission information is available at http://www.nature.com/reprints

Publisher's note Springer Nature remains neutral with regard to jurisdictional claims in published maps and institutional affiliations.